

An Epitaxial Ferroelectric Tunnel Junction on Silicon

Zhipeng Li, Xiao Guo, Hui-Bin Lu,* Zaoli Zhang, Dongsheng Song, Shaobo Cheng, Michel Bosman,* Jing Zhu, Zhili Dong, and Weiguang Zhu*

The pursuit of non-volatile memory devices on silicon with high storage density, high speed and low power consumption has been an important driving force for the study of new materials and designs of nanoscale architectures.^[1] Flash memory is currently the main commercialized non-volatile memory in embedded chips.^[2] However, flash has some drawbacks, such as long programming times, limited cycle endurance and high programming voltages (around 10 V). A number of alternative memory technologies, namely magnetic random access memory (MRAM) and ferroelectric RAM (FeRAM) have achieved higher programming performance than flash, but scaling-down these technologies remains challenging.^[3,4] Recently, ferroelectric tunnel junction (FTJ) devices emerged as an alternative memory technology, attracting much attention of solid-state physicists and materials scientists. Conceptualized in the 1970s by Esaki et al.,^[5] it has been experimentally demonstrated that when an ultrathin ferroelectric film serves as barrier layer in tunnel junction devices, the quantum-mechanical tunneling current and resistance can be manipulated non-destructively via the polarization direction of the ferroelectric

barrier, an effect known as the tunneling electroresistance (TER) effect.^[6–9] An FTJ device can achieve two conductance states with a ratio as high as two orders of magnitude, as well as memory programming with a short voltage pulse (10 ns) and at modest current densities ($\sim 1 \times 10^4$ A cm⁻²). In addition, FTJ devices have the potential to function as nanometer-scale non-volatile memory devices, operating with low power consumption.^[7,10] Nonetheless, FTJ devices with nearly ideal characteristics have only been demonstrated on perovskite heterostructures that were deposited on closely lattice-matched, *non-silicon* substrates such as SrTiO₃ (STO) and NdGaO₃.^[6–9] Although these substrates can provide compressive strain to the ferroelectric BaTiO₃ (BTO), achieving room temperature ferroelectricity and possibly the TER effect in layers only a few nanometer thick, they are not compatible with the ubiquitous microfabrication technologies based on the silicon platform. This has so far limited the application of FTJs as memory technology.

In this work, we demonstrate epitaxial FTJ devices with the TER effect on Si(001) wafers, fabricated by pulsed laser deposition (PLD). This is accomplished by including a thin layer of STO as an epitaxial template on silicon. Using transmission electron microscopy (TEM), scanning TEM (STEM) high angle angular dark field (HAADF) imaging, and electron energy loss spectroscopy (EELS), we demonstrate near-atomically sharp chemical interfaces with *c*-axis orientation in the perovskite heterostructures. Enhanced tetragonality (*c/a*) and room temperature ferroelectricity in ultrathin BTO are revealed by aberration-corrected high resolution TEM (HRTEM) and piezoelectric force microscopy (PFM), respectively. Using conductive AFM, the polarization switching-induced change in tunneling resistance is measured to be two orders of magnitude. This resistive switching behavior is further verified using a model based on tunneling currents through a trapezoidal potential barrier whose profile can be modulated by polarization switching.

The epitaxial La_{0.7}Sr_{0.3}MnO₃ (LSMO) and 3.2 nm thick BTO films used in this work were grown by pulsed laser deposition on silicon wafer using an STO buffer layer. **Figure 1a** presents the LSMO/BTO heterostructure and corresponding atomic-resolution STEM-HAADF image of the cross-sectional sample. As the HAADF intensity is proportional to the local atomic number ($\sim Z^{1.7}$), the different chemical layers can be identified. The BTO barrier layer is confirmed to be 8 unit cell thick. The HAADF image and intensity profile in **Figure 1b** demonstrate near-atomically sharp interfaces in the STO/LSMO/BTO stack, suggesting that cationic mixing at the interfaces is minimal. In addition, the conventional HRTEM image in **Figure 1c** presents the *c*-axis oriented epitaxial perovskite stacks with BTO and LSMO thickness of ~ 3.2 nm and 13.3 nm, respectively.

Dr. Z. Li, X. Guo, Prof. W. Zhu
School of Electrical and Electronic Engineering
Nanyang Technological University
Singapore 639798, Singapore
E-mail: ewzhu@ntu.edu.sg



Prof. H.-B. Lu
Beijing National Laboratory for Condensed Matter Physics
Institute of Physics, Chinese Academy of Science
Beijing 100190, China
E-mail: hblu@iphy.ac.cn

Dr. M. Bosman
Institute of Materials Research and Engineering
Agency for Science, Technology and Research (A*STAR), 3 Research Link
Singapore 117602, Singapore
E-mail: michel.bosman@gmail.com

Prof. Z. Dong
School of Materials Science and Engineering
Nanyang Technological University
Singapore 639798, Singapore

Dr. Z. Zhang
Erich Schmid Institute of Materials Science
Austria Academy of Sciences
A-8700, Leoben, Austria

Dr. Z. Li, D. Song, S. Cheng, Prof. J. Zhu
Beijing National Center for Electron Microscopy
School of Materials Science and Engineering
The State Key Laboratory of New Ceramics and Fine Processing,
Laboratory of Advanced Materials (MOE)
Tsinghua University
Beijing 100084, People's Republic of China

DOI: 10.1002/adma.201402527

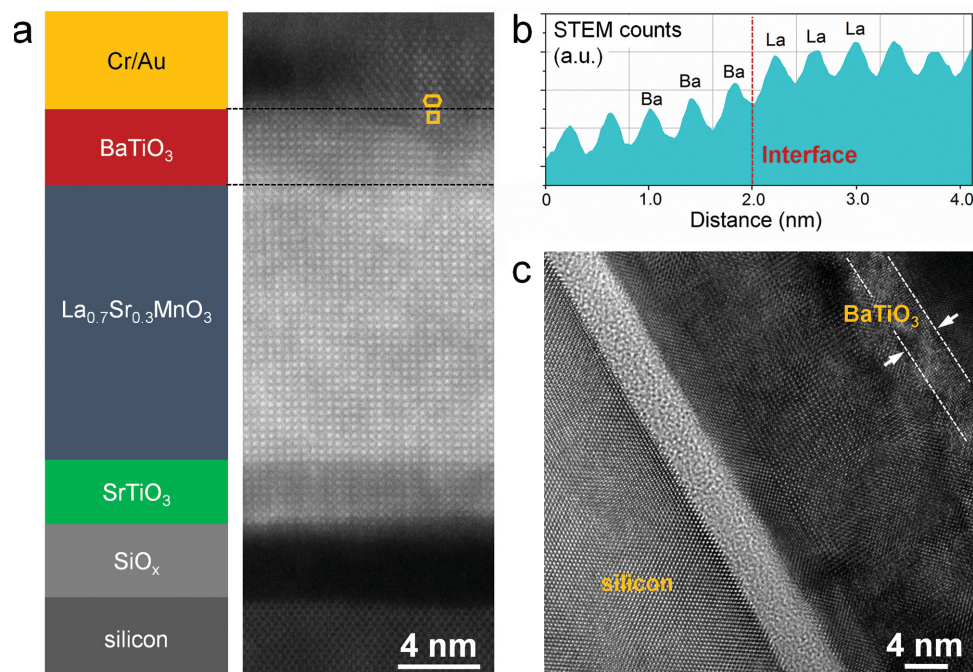


Figure 1. STEM and TEM on the Si/SiO_x/STO/LSMO/BTO stacks. a) A STEM-HAADF image and corresponding configuration of the stacks; the black dashed lines indicate the position of the BTO film. The metal protection layer with closed-packed structure can be identified on top of the perovskite BTO, as marked by the yellow hexagonal (metal side) and cubic (BTO side) units. b) HAADF averaged intensity profile across the LSMO/BTO interface. c) A lattice image in TEM mode; the dashed lines and arrows indicate the location of the BTO layer.

Figure 1c also shows that the layer between the silicon and the STO is amorphous. As was shown earlier in experiments that used molecular beam epitaxy (MBE, instead of our PLD) as growth technique,^[11] such an amorphous layer forms when silicon reacts with the oxygen from the epitaxially grown STO; in the Supporting Information (Figure S3c), we demonstrate that this amorphous layer consists of SiO₂. The X-ray diffraction (XRD) θ -2 θ scan of the Si/STO/LSMO/BTO stack confirms the TEM results, indicating monocrystallinity and *c*-axis orientation of the perovskite films on (001) silicon (Supporting Figure S1). From selected area electron diffraction (SAED), the crystal orientation is determined as perovskite (100)|| silicon (110), which shows that the perovskite orientation is rotated in-plane by 45° with respect to the silicon crystal (Supporting Figure S2). These results are similar to the epitaxial perovskite films on silicon grown by MBE.^[12,13] The average in-plane lattice parameter of perovskite films measured by SAED is 0.391 ± 0.005 nm which is smaller than that of bulk BTO (0.399 nm), suggesting possible strain enhancement of ferroelectricity in ultrathin BTO.

Typically, the epitaxial strain and polarization in ferroelectric materials are coupled, leading to a direct relationship between polarization and tetragonality (*c/a*).^[14,15] To quantitatively study the degree of tetragonality in the BTO barrier layer, spherical aberration-corrected HRTEM with sub-Angstrom resolution is used. A HRTEM image of ultrathin BTO on the [010] zone axis with multislice-simulated atom positions is shown in **Figure 2a**. The accurate positions (coordination) of cation columns are determined by means of a least-squares fit of the individual contrast minima by Gaussian intensity profiles, and the positions of contrast minima are regarded as the peak centroids. The lattice parameters *a* and *c* can then be extracted from the

coordination of the cation columns.^[16] Figure 2b presents a unit-cell scale mapping of tetragonality *c/a* values in the BTO film from an area of 21 unit cells along the in-plane direction by 8 unit cells along the out-of-plane direction. It can be seen that the spatial distribution of tetragonality values is quite uniform in BTO. The tetragonality as a function of distance along the *c*-axis, shown in Figure 2c, plots the average values for each of the 8 rows of BTO unit cells, with the error bars indicating the 95% confidence interval. The tetragonality remains nearly constant around 1.045 from the LSMO/BTO interface to the BTO surface. Compared with the *c/a* value of bulk BTO (1.010), the tetragonality of this ultrathin BTO on LSMO grown on silicon is enhanced. The lattice constants of BTO are measured as *a* = 0.395 ± 0.005 nm and *c* = 0.413 ± 0.005 nm, with the corresponding compressive strain level +1.0% along the in-plane direction compared with the bulk BTO. The tetragonality value of BTO on our silicon platform is similar to the earlier published *c/a* = 1.051 obtained from 2 nm BTO grown on a NdGaO₃ substrate with an LSMO buffer, and larger than the *c/a* = 1.038 from BTO grown on DyScO₃ for *T_C* > 900 K.^[14,17] As epitaxial strain can also modify the crystal field-sensitive EELS fine structure,^[18,19] we confirm from the BTO EELS Ti *L*₃ edge energy splitting in Figure S3 that the BTO lattice is strained. In addition, the EELS fine structure of the BTO Ti-*L*_{2,3} edge is typical of Ti⁴⁺ cations, excluding the possibility of oxygen vacancies-driven formation of Ti³⁺ cations in BTO.^[20]

The surface topography of the Si/STO/LSMO/BTO is shown in **Figure 3a**. The roughness is ~300 pm, indicating an atomically smooth surface. Ferroelectric characterization is performed by PFM; Figures 3b and 3c show the out-of-plane PFM phase and amplitude images, respectively, of ferroelectric

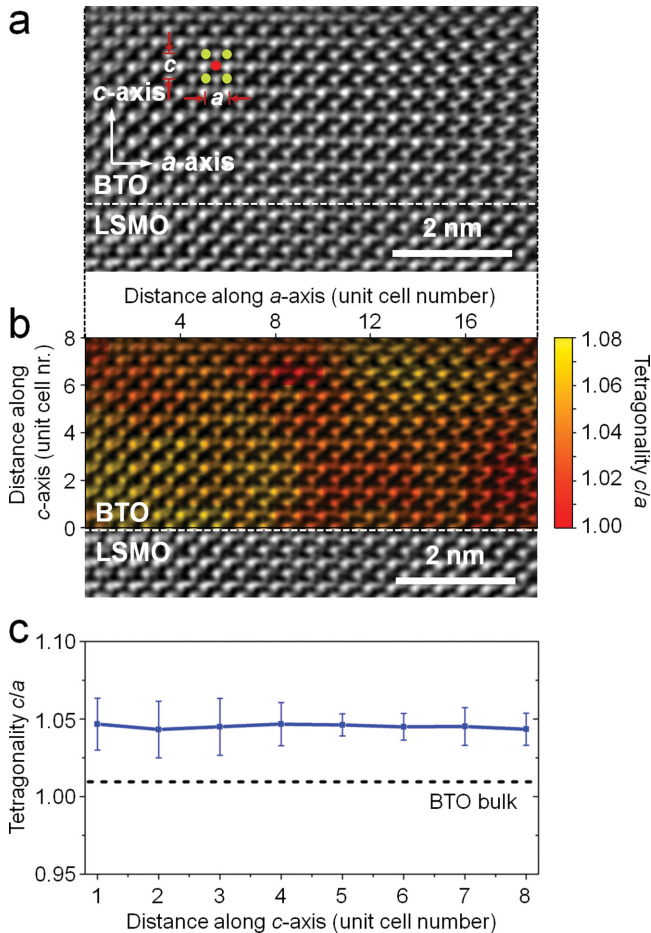


Figure 2. Tetragonality c/a measurement from HRTEM imaging. a) HRTEM taken by a spherical aberration-corrected TEM, the multislice-simulated positions of Ba (yellow spheres) and Ti (red spheres) are indicated. The simulation conditions include a defocus of -21 nm and sample thickness of 3.6 nm. The dashed line indicates the LSMO/BTO interface which is determined by comparing the corresponding HAADF-STEM image. b) Unit-cell scale mapping of the tetragonality of BTO. c) The distribution of BTO tetragonality as a function of distance from the LSMO/BTO interface (left in the plot) to the BTO surface (right). The dashed line indicates the tetragonality value of bulk BTO.

domains written on the 3.2 nm thick BTO. The antiparallel polarization is revealed by 180° phase contrast which can be observed without degradation for several hours. The PFM hysteresis loop in Figure 3d indicates the ferroelectric nature of the BTO layer. The coercive voltages are found to be -1.4 V and $+1.2$ V. The polarization-induced change of tunneling current is measured by the following approach that can show a new possibility of FTJs made on silicon: the voltage is applied to the bottom electrode, and contact is made through contacting a conductive AFM tip on the BTO film surface, measuring the current via conductive AFM.^[6,7,21] The ferroelectric polarization is first switched upward (pointing towards the AFM tip) or downward (pointing towards LSMO) by applying a dc voltage (V_{Write}) between the AFM tip and the bottom electrode, with $|V_{\text{Write}}| > V_C$, the latter being the coercive field. Subsequently, the corresponding tunnel current (I) is measured at low dc voltage, with V_{Read} sweeping from -250 mV to $+250$ mV, which

is below V_C . The measured $I-V_{\text{Read}}$ curves of BTO with opposite polarization states are shown in Figure 3e. Both are nonlinear and nearly symmetric, which is typical for a tunnel junction.^[6-9] These characteristics are very different from the $I-V$ curves of other resistive switching devices on silicon, where the switching is based on the formation of conductive filaments.^[22,23] In addition, the topographic images of the surface after the tunnel current measurements do not show any sign of pinhole formation which would be induced by dielectric breakdown. Following the work of Gruverman et al. and Chanthbouala et al.,^[6,7] we infer that the observed resistive switching behavior is caused by the ferroelectric polarization reversal. In case of our 3.2 nm thick BTO film, the currents reach 9.84×10^{-9} A and 4.63×10^{-11} A at the polarization down (ON) state and the up (OFF) state, respectively when the V_{Read} is 250 mV, giving a TER ratio of 212. The Hertz model is used here to estimate the area of AFM tip-sample contact, giving an approximate value of 105 nm².^[24] Then the measured tunneling currents in Figure 3e imply a current density J of 9×10^3 A/cm² and a sheet resistance of 2×10^3 $\Omega \cdot \mu\text{m}^2$ when $V_{\text{Read}} = 250$ mV in the ON state. These values are comparable with the experimental data of FTJ with a BTO barrier layer grown on perovskite substrates.^[7,25] A similar ON/OFF phenomenon induced by polarization reversal was also reported in a ferroelectric Schottky diode, however, the thickness of the ferroelectric layer was hundreds of nanometers and the current density around 10^{-3} A/cm².^[26] That value is several orders of magnitude smaller than what we obtained in this work, therefore, the ferroelectric Schottky diode mechanism can be excluded here. In addition, we performed a fatigue and endurance test of the resistive switching in this FTJ, the results are shown in Figure 3f. It is demonstrated that the ON/OFF ratio of about 200 in the FTJ on silicon can be maintained for up to at least 10 000 cycles.

Theoretically, the polarization reversal can change the density of states at BTO/electrodes interfaces and the electronic band structure of the barrier. To simulate the measured $I-V_{\text{Read}}$ curves and verify the mechanism of the observed resistive switching associated with polarization reversal, a model based on the TER effect is employed, involving a tunneling current through a trapezoidal potential barrier whose profile depends on polarization direction^[6,27] (details can be found in the Supporting Information). In the configuration of transport measurement, the LSMO bottom electrode and Pt-Ir top electrode (the AFM tip is coated with Pt-Ir alloy, so it is regarded as the top electrode of the BTO here) have different screening lengths, which leads to an asymmetry in the potential profiles of the junction. The barrier has a width of d and amplitudes of electrostatic potential at the LSMO/BTO and BTO/Pt-Ir interfaces of ϕ_1 and ϕ_2 , respectively. Figure 3e shows a fit of the experimental $I-V_{\text{Read}}$ curves for 3.2 nm thick BTO using the following parameters: $\phi_1 = 0.21$ eV and $\phi_2 = 0.71$ eV for polarization down (ON state), and $\phi_1 = 0.15$ eV and $\phi_2 = 1.43$ eV for polarization up (OFF state). The respective change in the potential energy profiles of the junction is schematized in Figure S4 in the Supporting Information. The potential energy difference $\phi_2 - \phi_1$ is adjusted from 0.5 eV to 1.28 eV due to polarization reversal in the down-to-up direction. The 0.78 eV change of $\phi_2 - \phi_1$ value in our experiments is close to that reported by Gruverman et al.^[6] This energy difference controls the asymmetry of the potential

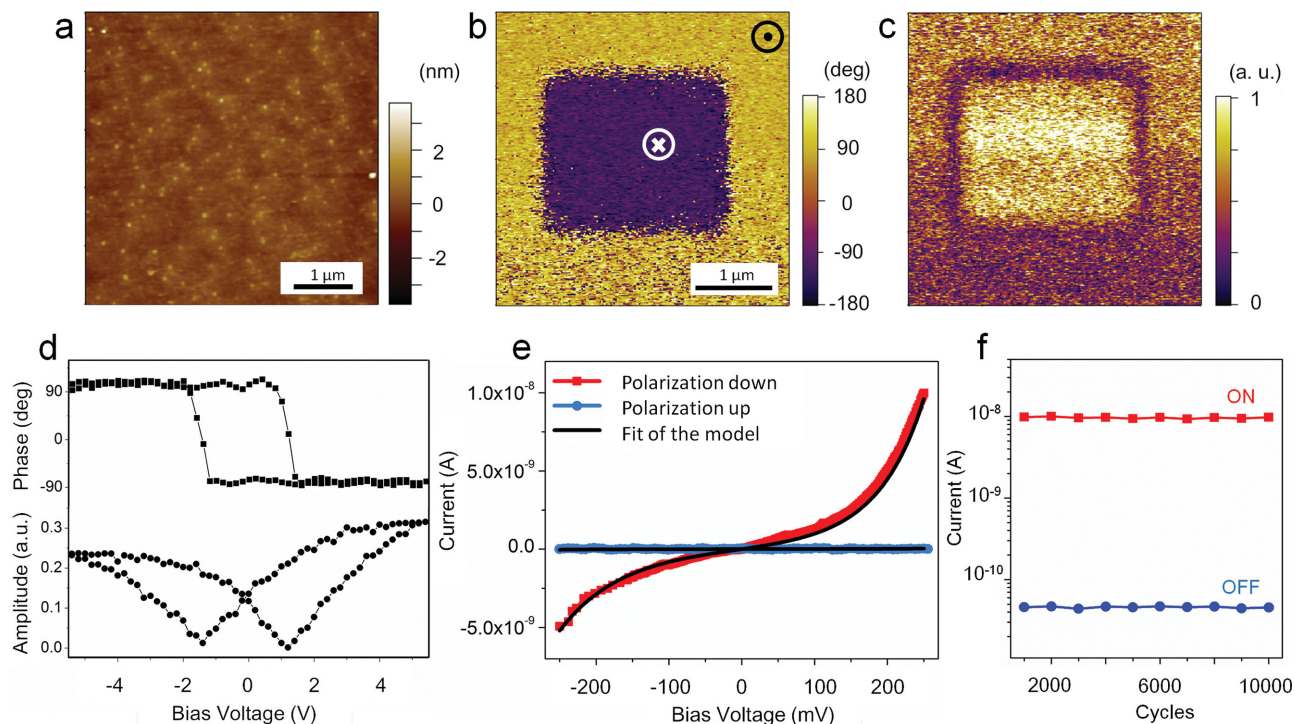


Figure 3. a) AFM topography of 3.2 nm thick BTO on LSMO/STO/silicon wafer. b) PFM out-of-plane image and c) amplitude image of the polarization pattern recorded after writing an area of $2 \times 2 \mu\text{m}^2$ square (polarization downwards in purple area and upwards in yellow area) with +3 V used as conductive tip bias. d) Local PFM hysteresis loops: top, phase signal; bottom, amplitude signal. e) I - V_{Read} curves of BTO with opposite polarization states measured by conductive AFM. The solid lines show the fit of our model to the experimental data. f) Bipolar resistive switching by cycling with ± 3 V voltage pulses.

profile and plays a decisive role in the resistance change due to the polarization reversal.^[28] Meanwhile, the average potential barrier height U_{Up} (0.79 eV) for the polarization up-state is larger than U_{Down} (0.46 eV) for polarization-down. This fact makes the conductance for polarization-down much larger than that for polarization-up, resulting in the observed TER effect.

Although the above results are measured from a non-optimized device, nanoscale ferroelectricity and the giant TER effect have been readily observed in our FTJ on silicon. Some key parameters of the junction, including the tetragonality and ferroelectricity of BTO, the TER ratio, current density and the modified potential barrier height are comparable with junctions grown on perovskite substrates. With this device built on silicon, the FTJ memory can be integrated with other microelectronic components to form integrated circuits. Furthermore, our design is expected to lead to nonvolatile memory units on silicon with four-state functionality, by using multiferroic materials as barrier layer,^[29] or utilizing the coupling effect between the ferroelectric layer and ferromagnetic electrodes.^[30]

In summary, we have demonstrated and verified the giant TER effect in silicon-based ferroelectric tunnel junction devices with 3.2 nm thick, epitaxial BTO. Enhancement of tetragonality and corresponding room-temperature ferroelectricity in the ultrathin BTO barrier layer are confirmed by both transmission electron microscopy techniques and piezoelectric force microscopy, respectively. Upon polarization reversal, the tunneling conductance changes by two orders of magnitude. Our results suggest the possibility of integrating FTJs as binary data storage

media in nonvolatile memory cells on silicon wafers, opening a door to greatly miniaturized silicon-based, non-volatile memory devices.

Experimental Section

The silicon substrates were first dipped into a ~5% HF solution for 20–30 s to remove the native silicon oxide on the surface and to form a hydrogen-terminated surface, followed by an immediate transfer into the PLD chamber. The deposition process of the perovskite films was performed using a KrF laser ($\lambda = 248$ nm) with a fluence of $2 \text{ J}/\text{cm}^2$ and repetition rate of 1 Hz. STO with a thickness of 3 nm was deposited on silicon substrates as buffer layers at room temperature under an oxygen pressure of $\sim 1 \times 10^{-4}$ Pa. The substrate temperature was then raised to 620 °C for the annealing process. An in-situ reflected high energy electron diffraction (RHEED) system and CCD camera were used to monitor the crystallization process of the STO layer. The RHEED streak pattern was observed when the STO was well-crystallized from amorphous to a c -axis oriented single crystal. Afterwards, LSMO, which worked as an electrode to facilitate electrical measurements, was subsequently deposited at a temperature of 780 °C under an oxygen pressure of 26 Pa, avoiding oxygen vacancies and cation non-stoichiometry during growth.^[31] The BTO was grown at 650 °C under an oxygen pressure of 7 Pa. The samples were annealed for 0.5 h at 650 °C and then cooled to room temperature, all under an oxygen pressure of 1000 Pa. A Rigaku Smartlab high-resolution diffractometer with copper X-ray generator tube was used for XRD measurements. Before TEM sample preparation, a Cr/Au layer was deposited on BTO, to protect the perovskite film from beam damage during ion milling. TEM specimens were prepared to electron transparency by grinding, dimpling, and ion milling in a Gatan

Precision Ion Polishing System. The specimens were cleaned briefly in an oxygen plasma, and then transferred directly into the microscopes for observation. An FEI Titan 80-300 TEM with Schottky emitter, operated at 200 kV was employed for Z-contrast imaging and EELS line scans with a probe diameter of 1 nm, in STEM mode. The TEM images of BTO for tetragonality analysis were taken by a conventional JEOL 2010F TEM and a JEOL 2100F TEM equipped with an imaging spherical aberration corrector.^[32] Scanning probe microscope experiments were conducted on a Cypher AFM from Asylum Research. Conductive Pt-Ir-coated silicon cantilevers (from NanoWorld Company) were used for piezoelectric force microscope (PFM) imaging and polarization switching studies. The ferroelectric hysteresis loops collected during polarization switching were measured in DART (dual a.c. resonance tracking) mode. Both phase and amplitude images were recorded in single-frequency PFM mode. The I–V characteristics of the tunnel junction were performed in conductive AFM (C-AFM) mode using a Keithley 6430 Source Meter connected with the sample holder. The bias voltage was applied to the LSMO bottom electrode and the AFM tip was grounded for all C-AFM measurements. In the fatigue and endurance test of the resistive switching, voltage was applied to the BTO with a square wave form of ± 3 V during cycling. After every 1000 cycles, the ON (polarization down)/OFF (polarization up) state was set by applying a 100 μ s voltage pulse of -3 V/ $+3$ V for the corresponding tunneling current measurements (with $V_{\text{Read}} = 250$ mV).

Supporting Information

Supporting Information is available from the Wiley Online Library or from the author.

Acknowledgements

The authors would like to thank the Science and Engineering Research Council (SERC) of Singapore Agency for Science, Technology and Research (A*STAR) for their financial support (Grant Number 102 101 0019) and the Office of China Postdoctoral Council for the scholarship under the International Postdoctoral Exchange Fellowship Program.

Received: June 6, 2014

Revised: July 11, 2014

Published online:

- [1] J. E. Brewer, M. Gill, *Nonvolatile Memory Technologies with Emphasis on Flash*, IEEE Press, NJ, USA, **2008**.
- [2] R. Bez, E. Emilio, A. Modelli, A. Visconti, *Proc. IEEE* **2003**, *91*, 489.
- [3] G. R. Fox, F. Chu, T. Davenport, *J. Vac. Sci. Technol. B* **2001**, *19*, 1967.
- [4] J. M. Daughton, A. V. Pohm, *J. Appl. Phys.* **2003**, *93*, 7304.
- [5] L. Esaki, R. B. Laibowitz, P. J. Stiles, *IBM Tech. Discl. Bull.* **1971**, *13*, 2161.
- [6] A. Gruverman, D. Wu, H. Lu, Y. Yang, H. W. Jang, C. M. Folkman, M. Ye. Zhuravlev, D. Felker, M. Rzechowski, C.-B. Eom, E. Y. Tsymbal, *Nano Lett.* **2009**, *9*, 3539.
- [7] A. Chanthbouala, A. Crassous, V. Garcia, K. Bouzheouane, S. Fusil, X. Moya, J. Allibe, B. Dlubak, J. Grollier, S. Xavier, C. Deranlot, A. Moshar, R. Proksch, N. D. Mathur, M. Bibes, A. Barthélemy, *Nat. Nanotechnol.* **2012**, *7*, 101.
- [8] Y. W. Yin, J. D. Burton, Y.-W. Kim, A. Y. Borisevich, S. J. Pennycook, S. M. Yang, T. W. Noh, A. Gruverman, X. G. Li, E. Y. Tsymbal, Q. Li, *Nat. Mater.* **2013**, *12*, 397.
- [9] Z. Wen, C. Li, D. Wu, A. Li, N. Ming, *Nat. Mater.* **2013**, *12*, 617.
- [10] E. Y. Tsymbal, A. Gruverman, V. Garcia, M. Bibes, A. Barthélemy, *MRS Bull.* **2012**, *37*, 138.
- [11] C. Dubourdieu, J. Bruley, T. M. Arruda, A. Posadas, J. Jordan-Sweet, M. M. Frank, E. Cartier, D. J. Frank, S. V. Kalinin, A. A. Demkov, V. Narayanan, *Nat. Nanotechnol.* **2013**, *8*, 748.
- [12] R. A. McKee, F. J. Walker, M. F. Chisholm, *Phys. Rev. Lett.* **1998**, *81*, 3014.
- [13] S.-H. Baek, C.-B. Eom, *Acta Mater.* **2013**, *61*, 2734.
- [14] K. J. Choi, M. Biegalski, Y. L. Li, A. Sharan, J. Schubert, R. Uecker, P. Reiche, Y. B. Chen, X. Q. Pan, V. Gopalan, L.-Q. Chen, D. G. Schlom, C. B. Eom, *Science* **2004**, *306*, 1005.
- [15] D. G. Schlom, L.-Q. Chen, C.-B. Eom, K. M. Rabe, S. K. Streiffer, J.-M. Triscone, *Annu. Rev. Mater. Res.* **2007**, *37*, 589-626.
- [16] C.-L. Jia, V. Nagarajan, J.-Q. He, L. Houben, T. Zhao, R. Ramesh, K. Urban, R. Waser, *Nat. Mater.* **2007**, *6*, 64.
- [17] V. Garcia, S. Fusil, K. Bouzheouane, S. Enouz-Vedrenne, N. D. Mathur, A. Barthélemy, M. Bibes, *Nature* **2009**, *460*, 81.
- [18] J. Zhang, A. Visinoui, F. Heyroth, F. Syrowatka, M. Alexe, D. Hesse, H. S. Leipner, *Phys. Rev. B* **2005**, *71*, 064108.
- [19] G.-Z. Zhu, G. Radtke, G. A. Botton, *Nature* **2012**, *490*, 384.
- [20] L. Bocher, A. Gloter, A. Crassous, V. Garcia, K. March, A. Zobelli, S. Valencia, S. Enouz-Vedrenne, X. Moya, N. Mathur, C. Deranlot, S. Fusil, K. Bouzheouane, M. Bibes, A. Barthélemy, C. Colliex, O. Stéphan, *Nano Lett.* **2012**, *12*, 376.
- [21] H. Lu, D. J. Kim, C.-W. Bark, S. Ryu, C. B. Eom, E. Y. Tsymbal, A. Gruverman, *Nano Lett.* **2012**, *12*, 6289.
- [22] S. H. Jo, K.-H. Kim, W. Lu, *Nano Lett.* **2009**, *9*, 870.
- [23] X. Wu, D. Cha, M. Bosman, N. Raghavan, D. B. Migas, V. E. Borisenko, X.-X. Zhang, K. Li, K.-L. Pey, *J. Appl. Phys.* **2013**, *113*, 114503.
- [24] K. L. Johnson, *Contact Mechanics*, Cambridge University Press, United Kingdom, **1985**.
- [25] A. Chanthbouala, V. Garcia, R. O. Cherifi, K. Bouzheouane, S. Fusil, X. Moya, S. Xavier, H. Yamada, C. Deranlot, N. D. Mathur, M. Bibes, A. Barthélemy, J. Grollier, *Nat. Mater.* **2012**, *11*, 860.
- [26] P. W. M. Blom, R. M. Wolf, J. F. M. Cillessen, M. P. C. M. Krijn, *Phys. Rev. Lett.* **1994**, *73*, 2107.
- [27] M. Y. Zhuravlev, R. F. Sabirianov, S. S. Jaswal, E. Y. Tsymbal, *Phys. Rev. Lett.* **2005**, *94*, 246802.
- [28] Y. Zheng, W. J. Chen, X. Luo, B. Wang, C. H. Woo, *Acta Mater.* **2012**, *60*, 1857.
- [29] M. Gajek, M. Bibes, S. Fusil, K. Bouzheouane, J. Fontcuberta, A. Barthélemy, A. Fert, *Nat. Mater.* **2007**, *6*, 296.
- [30] V. Garcia, M. Bibes, L. Bocher, S. Valencia, F. Kronast, A. Crassous, X. Moya, S. Enouz-Vedrenne, A. Gloter, D. Imhoff, C. Deranlot, N. D. Mathur, S. Fusil, K. Bouzheouane and A. Barthélemy, *Science* **2010**, *327*, 1106.
- [31] Z. Li, M. Bosman, Z. Yang, P. Ren, L. Wang, L. Cao, X. Yu, C. Ke, M. B. H. Breese, A. Rusydi, W. Zhu, Z. Dong, Y. L. Foo, *Adv. Funct. Mater.* **2012**, *22*, 4312.
- [32] Z. Zhang, B. Rashkova, G. Dehm, P. Lazar, J. Redinger, R. Podloucky, *Phys. Rev. B* **2010**, *82*, 060103(R).